ELSEVIER

Electrically powered repeatable air explosions using microtubular graphene assemblies

Fabian Schütt [1,†,*], Florian Rasch [1,†], Nipon Deka [1], Armin Reimers [1], Lena M. Saure [1], Sören Kaps [1], Jannik Rank [1], Jürgen Carstensen [1], Yogendra Kumar Mishra [2], Diego Misseroni [4], Adrian Romani Vázquez [3], Martin R. Lohe [3,5], Ali Shaygan Nia [3], Nicola M. Pugno [4,6], Xinliang Feng [3], Rainer Adelung [1,*]

[1] Functional Nanomaterials, Institute for Materials Science, Kiel University, Kaiser Str. 2, 24143 Kiel, Germany
[2] Mads Clausen Institute, NanoSYD, University of Southern Denmark, Alsion 2, 6400 Sønderborg, Denmark
[3] Department of Chemistry and Food Chemistry, Center for Advancing Electronics Dresden (cfaed), Technische Universität Dresden, 01062 Dresden, Germany
[4] Laboratory of Bio-Inspired and Graphene Nanomechanics, Department of Civil, Environmental and Mechanical Engineering, University of Trento, via Mesiano 77, I-38123 Trento, Italy
[5] Sixonia Tech GmbH, Pestitzer Str. 16, 01187 Dresden, Germany
[6] School of Engineering and Materials Science, Queen Mary University of London, Mile End Road, London E1 4NS, UK

Controllable rapid expansion and activation of gases is important for a variety of applications, including combustion engines, thrusters, actuators, catalysis, and sensors. Typically, the activation of macroscopic gas volumes is based on ultra-fast chemical reactions, which require fuel and are irreversible. An "electrically powered explosion", i.e., the rapid increase in temperature of a macroscopic relevant gas volume induced by an electrical power pulse, is a feasible repeatable and clean alternative, providing adaptable non-chemical power on demand. Till now, the fundamental problem was to find an efficient transducer material that converts electrical energy into an immediate temperature increase of a sufficient gas volume. To overcome these limitations, we developed electrically powered repeatable air explosions (EPRAE) based on free-standing graphene layers of nanoscale thickness in the form of microtubes that are interconnected to a macroscopic framework. These low-density and highly permeable graphene foams are characterized by heat capacities comparable to air. The EPRAE process facilitates cyclic heating of cm^3-sized air volumes to several 100 °C for more than 100,000 cycles, heating rates beyond 300,000 K s^{-1} and repetition rates of several Hz. It enables pneumatic actuators with the highest observed output power densities (>40 kW kg^{-1}) and strains ~100%, as well as tunable microfluidic pumps, gas flowmeters, thermophones, and micro-thrusters.

Introduction

Explosions, although generally considered destructive, offer an efficient way to convert potential (usually chemical) energy into kinetic energy in a gas within a short time [1,2]. In general, an explosion is defined as the sum of the phenomena that occur during a local rapid release of energy. In addition, the release of energy must be sufficiently rapid and concentrated to produce an audible pressure wave [3]. The released energy is locally converted into a temperature rise causing an overpressure, leading

* Corresponding authors.
E-mail addresses: Schütt, F. (fas@tf.uni-kiel.de), Adelung, R. (ra@tf.uni-kiel.de).
† Shared first authorship.

https://doi.org/10.1016/j.mattod.2021.03.010

to an excess energy density that is degraded through heat transport and volume work in the environment [1,2].

However, even though such chemical explosions are widely used, they always require fuel and are irreversible [4], as fuel is consumed. In contrast to that, an "electrical explosion", i.e., the rapid increase in temperature of a macroscopic gas volume induced by an electrical power pulse, could be a feasible repeatable and clean alternative. Till now, the fundamental problem was to find a suitable transducer material, fulfilling the following criteria: (I) high and open porosity in order to contain large gas volumes (II) rapid volumetric Joule heating (coefficient of performance of ~1.0 [5]) with rates well beyond 100,000 K s^{-1}, (III) rapid (~ms) heat transfer from the transducer material to a large gas volume provided by a high volumetric surface area and (IV) resistance to high temperatures (up to several 100 °C) and temperature fluctuations. Additionally, (V) the volumetric heat capacity of the transducer material needs to be in the order of that of gases to allow for sufficiently fast heating and cooling rates and, therefore, high frequencies (explosions per second). Traditional Joule-heating technologies, such as radiant heaters, convection heaters, or fan heaters, do not fulfil all the described requirements, as they are typically based on bulk metal wires.

Recently, macroscopic three-dimensional (3D) carbon nanomaterial assemblies have been shown to hold great promise for Joule heating applications [6–8], e.g., gas sensing [9], throughflow heaters [10], loudspeakers [11–13], air filtration [14], bolometers [15], or clean-up of viscous crude oil [16]. They offer the possibility to utilize the exceptional properties of carbon nanomaterials, such as graphene [17], on the macroscopic scale, while not being limited by any underlying substrate [18]. However, with reported heating rates in the order of 10 K s^{-1} and an unfavorable nano- and microstructural arrangement of the used carbon nanomaterials assemblies (i.e., Knudsen Number ≥ 1), they were far from fulfilling the above-mentioned criteria needed for an efficient transducer material that is capable of carrying out a multitude of electrically powered explosions.

Here, we use graphene-based framework–aeromaterials (F-AMs) for electrically powered repeatable air explosions (EPRAE), with heating, cooling, and repetition rates of ~10^5 K s^{-1}, ~10^4 K s^{-1}, and ~10 Hz, respectively (Fig. 1). As illustrated in Fig. 1a, the employed F-AMs feature an interconnected network of hollow exfoliated graphene (EG) or reduced graphene oxide (rGO) microtubes with a nanoscopic wall thickness (<25 nm) [19]. The open-porous (~99.9%) structure and low density (~2–20 mg cm^{-3}) of the F-AMs result in an ultra-low volumetric heat capacity (between 1 to 5 kJ m^{-3} K^{-1}, Supplementary Text S1) similar to that of air, a high and fully accessible volumetric surface area (~0.14 m^2 cm^{-3}, Supplementary Text S2), and mechanical robustness [19,20], in which the properties of the gaseous phase can be estimated to that of free gas (Knudsen number $\ll 1$). This extraordinary set of properties of the F-AMs forms the basis of the EPRAE concept.

The idealized thermodynamic processes of the EPRAE concept are schematically illustrated in Fig. 1b. While air was used as the working gas in this study, the concept is also valid for other gases, such as nitrogen or argon. In the first step (state 1 → 2), heat is rapidly and uniformly transferred to the gas contained inside the F-AMs by fast (<1 ms) Joule heating of the F-AMs. This results in a fast increase in the kinetic energy of the gas molecules contained inside the F-AMs and, thus, an increase in the pressure of the system. The second step (state 2 → 3) involves a rapid (~1 ms) adiabatic expansion of the gas back to the equilibrium pressure (the actual explosion), followed by an isobaric heat rejection (state 3 → 1) to the starting volume and temperature in around 200 ms. Such a thermodynamic cycle is also referred to as the Lenoir cycle [21], which is used as a model to describe the thermodynamics of the first commercially produced combustion engine, invented in 1860. A series of several EPRAEs can be seen (and heard) in the Video S1.

While a fast heat transfer from the F-AMs to the gas is given by their large volumetric surface area, the open-porous framework structure is key for the EPRAE concept, as it allows for a fast heat transfer by convection and, thus, rapid (<10 ms) and large (e.g., 200%) volume expansions, without causing any structural damage to the F-AMs during operation. In contrast to conventional gas activation systems, such as blowers, gas pumps, fans, heating wires or hotplates, the EPRAE concept enables the rapid activation of arbitrarily scalable gas volumes (from litres to nanolitres), based on the size of the F-AM and the amount of electrical energy used. Additionally, as no chemical reaction is involved, the process is environmentally friendly, repeatable and can be conducted with relatively low voltages/currents and high repetition rates (~10 Hz) as a sequence of explosions (Fig. 1c, corresponding voltage/current profiles in Fig. S1). We demonstrate that EPRAE can be exploited for different applications, such as the fabrication of a novel class of fluidic pumps (e.g., for microfluidic systems), extremely fast pneumatic micro and macro actuators (e.g., for soft robotics, tactile displays, shock absorber systems), thermophones, micro-thrusters, as well as highly sensitive gas flowmeters.

Results and discussion

Fabrication and characterization of F-AMs

The employed F-AMs were fabricated as described elsewhere [19,22] (Materials and Methods and Supplementary Figs. S2 and S3). In short, highly porous (~94%) networks of interconnected tetrapod-shaped zinc oxide (t-ZnO) microparticles [23] (Fig. S2) were infiltrated with water-processable EG or graphene oxide (GO) dispersions, resulting in a homogenous coating of the template material with a thin (<25 nm) layer of the nanomaterials. Afterwards, the t-ZnO templates were removed by HCl etching and the GO-based samples were chemically reduced with ascorbic acid to obtain rGO networks. Finally, the samples were washed with deionized water and transferred to absolute ethanol for critical point drying (Fig. S3).

The resulting macroscopic structures have a cylindrical geometry with high uniformity in size (6 mm in diameter and height) and consist of a network of interconnected hollow microtubes with a mean length of ~25 μm, a diameter of ~2 μm and a wall thickness of ~25 nm, as shown in Fig. 2a and b. It should be noted that a large fraction of the microtubes does not completely retain the hexagonal morphology of the ZnO tetrapod arms and shows a more roundish shape after etching and drying (Fig. 2b). However, this does not affect the mechanical integrity and the microstructure of the samples. In the following, the F-AMs pro-

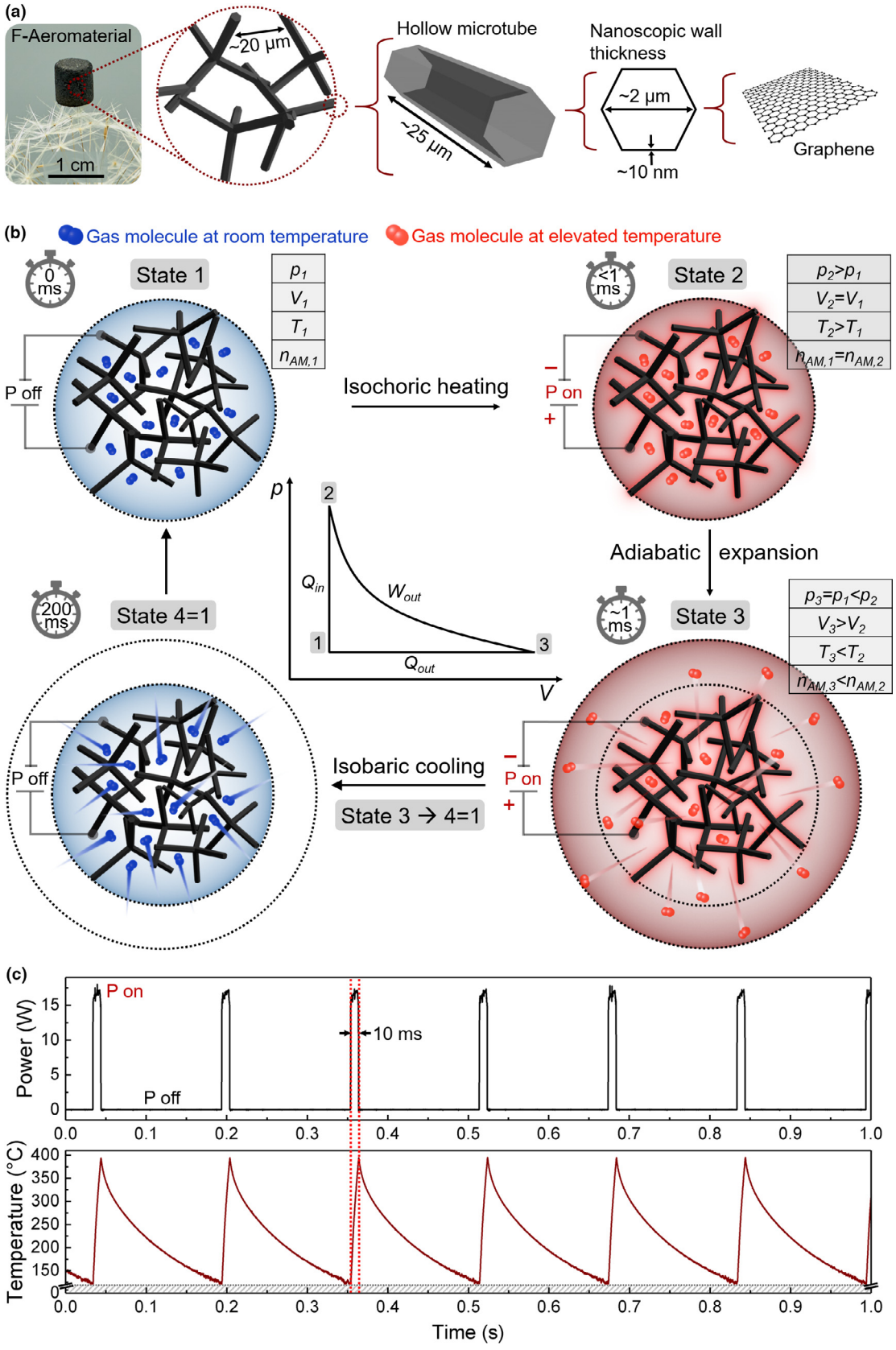

FIGURE 1

Electrically powered repeatable air explosions (EPRAE). (a) Photograph of highly porous (99.9%) graphene-based framework aeromaterial (F-AM), consisting of interconnected, hollow graphene microtubes (~25 μm in length, ~2 μm in diameter) with nanoscopic wall thickness (~10 nm). (b) Idealized thermodynamic cycle of the EPRAE concept, involving an isochoric rapid (<1 ms) heat addition to the gas (state 1 → 2) by Joule heating of the F-AMs causing a pressure increase, followed by a rapid adiabatic expansion of the gas (state 2 → 3) back to its original pressure and a final isobaric heat rejection (state 3 → 1) to its original volume and temperature. Please note that the schematic is not to scale – the size of the molecules is several orders of magnitude smaller than the pore size of the F-AM. (c) Typical EPRAE temperature–time profile (bottom), induced by 10 ms power pulses (peak power ~18 W) at a repetition rate of ~6.7 Hz (top).

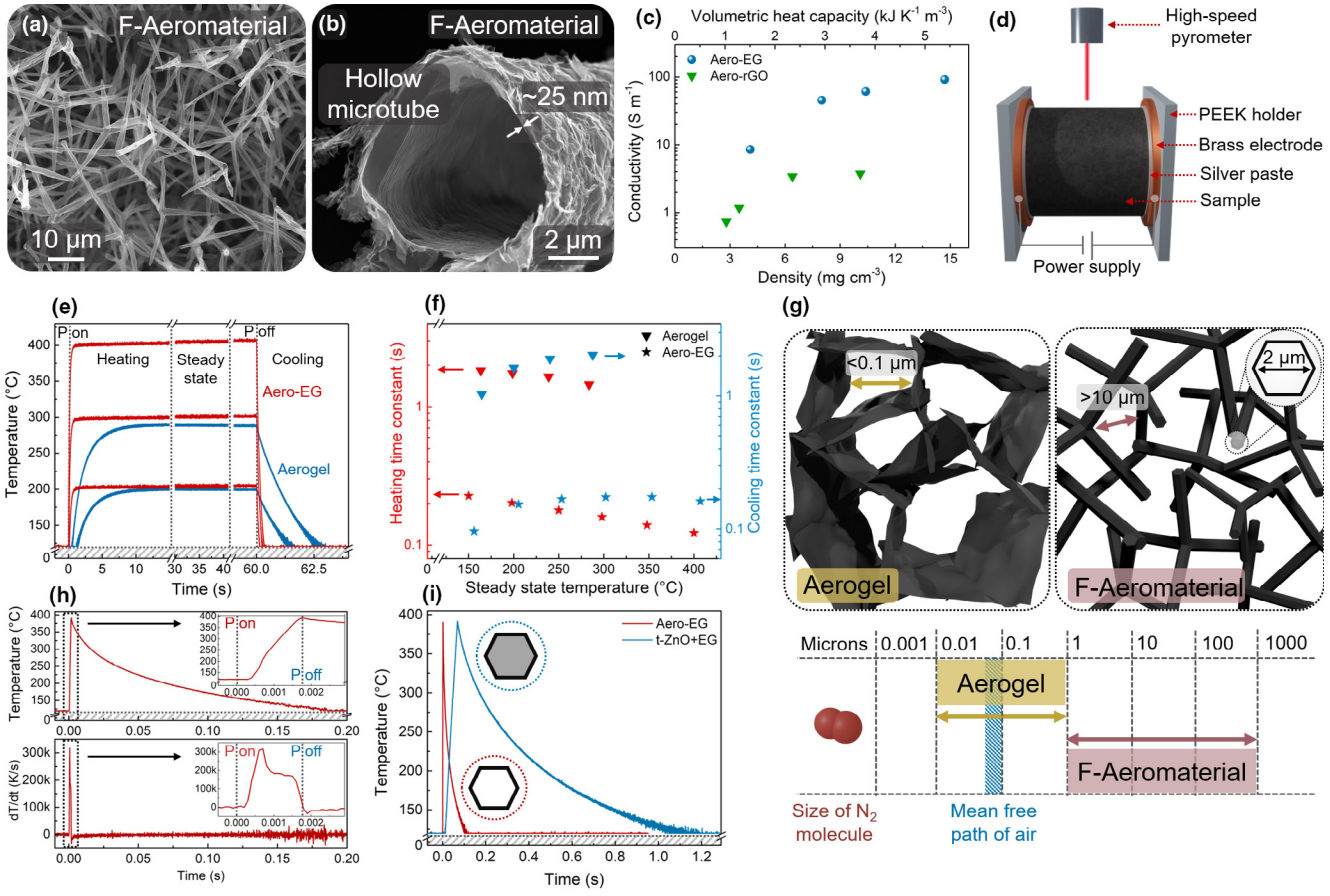

FIGURE 2

Microstructure and properties of F-AMs. (a) and (b) Representative SEM images of the F-AMs, revealing the framework structure with hollow, interconnected microtubes and high open porosity. (c) Conductivity versus F-AM density/volumetric heat capacity for Aero-EG and Aero-rGO. (d) Schematic of setup for investigation of Joule-heating and cooling characteristics of the F-AMs and the graphene aerogel. (e) Steady-state Joule-heating and cooling characteristics of Aero-EG and a graphene aerogel for different applied powers (details in Fig. S7). (f) Heating and cooling time constants for Aero-EG and the aerogel, obtained from the steady-state Joule-heating temperature–time profiles shown in e and Fig. S6. (g) Schematic of the structural morphologies of a typical graphene aerogel and a F-AM, respectively. As denoted in the diagram, the length scales of the pore sizes in the F-AM are more than two orders of magnitude larger than the mean free path of air, whereas the latter is in the same order or above typical pore sizes in the aerogel. (h) Non-steady-state Joule-heating and cooling characteristics of Aero-EG after inducing a short (1.7 ms) power pulse (152 W), showing the temperature–time profile (top) and its derivative (bottom). The latter shows the heating and cooling rates as a function of time. (i) Comparison of temperature–time profiles for Aero-EG and EG-coated t-ZnO network after inducing short power pulses to the samples (2.1 ms and 69.2 ms).

duced from rGO and EG are labeled as Aero-rGO and Aero-EG, respectively. The electrical conductivity of the F-AMs can be adjusted by increasing the amount of deposited EG and GO flakes on the sacrificial templates. Fig. 2c shows that the electrical conductivity of Aero-EG and Aero-rGO increased almost linearly with the density, reaching maximum values of around 90 S m^{-1} and 3 S m^{-1} for Aero-EG (14 mg cm^3) and Aero-rGO (10 mg cm^3), respectively. The higher conductivity of Aero-EG indicates the high quality of the employed EG sheets, which is also confirmed by the low D/G band intensity ratio determined by Raman microscopy (Fig. S4).

Steady-state Joule-heating and cooling characteristics of F-AMs

The Joule-heating and cooling characteristics of the F-AMs were investigated by a high-speed pyrometer working in the temperature range between 120 °C and 550 °C (more details in Materials and Methods). As schematically shown in Fig. 2d, the F-AMs were contacted with conductive silver paste between two brass electrodes and placed in the focus of the pyrometer. To investigate the complete temperature range during Joule heating and cooling of the F-AMs, the temperature profiles were additionally measured with an infrared camera (Figs. S5 and S6). Fig. 2e demonstrates the difference in the steady-state Joule heating characteristics of both Aero-EG and a classical graphene aerogel (prepared via chemical reduction of a GO dispersion [24], details in Materials and Methods) for different applied input powers (1–5 W) over a time period of one minute. The steady-state temperature of Aero-EG increases almost linearly with applied input power (Fig. S7), with a heating performance (dT dP^{-1}) of 83 K W^{-1}, similar to what was reported for carbon nanomaterial thin film heaters [25,26] and aerogels [6]. Additional temperature profiles for Aero-rGO, Aero-EG, and the aerogel are shown in Fig. S7 together with the corresponding heating performance. The difference in the Joule-heating and cooling behavior of the F-AMs and the graphene aerogels in Fig. 2e is best described by

their thermal time constants (τ_H for heating and τ_C for cooling) as a function of steady-state temperature, Fig. 2f (more details in Fig. S8 and Supplementary Text S3). Both τ_H and τ_C were around one order of magnitude lower for the F-AMs when compared to the classical aerogels, with values on the order of 10^{-1} s, even though their density (~10 mg cm^{-3}), electrical conductivity (~30 S m^{-1}) as well as volumetric heat capacity (~3 kJ m^{-3} K^{-1}, Supplementary Text S1) are on the same order of magnitude. The differences in τ_H and τ_C are directly related to the dissimilar micro- and nanostructure of the F-AMs compared to the aerogels (Fig. 2g and SEM images in Fig. S9), which strongly affects the heat transport within the structures. In general, the heat transport within non-evacuated porous materials is based on three mechanisms [27]: (I) heat conduction via the solid backbone, (II) diffusive heat transfer within the gaseous phase present in the open-porous structure, and (III) radiative heat transfer. The heat transfer through the carbon backbone of highly porous graphene aerogels has been shown to be extremely low, with thermal conductivities equivalent to 80% of air [28]. Furthermore, the radiative heat transfer in carbon nanomaterial aerogels is negligible [27]. Thus, heat transfer by the diffusion of gases is the dominant mechanism, which is characterized by the Knudsen number (Kn):

$$Kn = \frac{l_g}{D} \quad (1)$$

where l_g denotes the mean free path length of gas molecules and D is the effective pore dimension [27,29]. At standard pressure and room temperature, the mean free path of air is close to 68 nm [30]. In the case of classical graphene aerogels, the nanosheets are homogenously dispersed throughout the macroscopic volume with characteristic pore sizes well below the micron range (schematic in Fig. 2g), yielding values of Kn close to 1. Therefore, the heat transfer via the gaseous phase is strongly reduced within the aerogel. In contrast, in the case of the here employed F-AMs, the nanosheets are inhomogeneously distributed throughout the entire volume in the form of hollow microtubes, with a mean distance between the individual elements (hollow microtubes) of several tens of micrometers. The framework morphology of the F-AMs results in $Kn \ll 1$, since the mean free path of the gas molecules is 2–3 orders of magnitude smaller than the effective pore size [30]. The heat transfer in the F-AMs can, thus, be approximated by that of the free gas, with the gas molecules predominantly colliding with each other [27]. The almost undisturbed heat transfer via the gaseous phase enables the F-AMs to reach steady-state Joule-heating conditions almost instantaneously, resulting in mean heating and cooling rates superior to that of classical aerogels [6] by at least one order of magnitude (Fig. S10). All in all, the combination of several structural properties is important to realize the demonstrated fast heating and cooling rates, including a low volumetric heat capacity similar to that of the surrounding gas, a high and open porosity, and an appropriate distance between the carbon-based structural elements which act as heating elements.

Electrically powered repeatable air explosions (EPRAE)

These characteristics enable the F-AMs to be used as an efficient transducer material capable of rapidly converting electrical energy into heat of cm^3-sized gas volumes at high repetition rates, resulting in electrically powered repeatable air explosions (EPRAEs). The corresponding Joule-heating and cooling characteristics of the EPRAE process were characterized by applying short (1 ms up to 100 ms) power pulses to the F-AMs. Fig. 2h (top) shows the temperature–time profile of an Aero-EG sample (density ~8 mg cm^{-3}, conductivity ~35 S m^{-1}) induced by a 1.7 ms power pulse width of 640 W cm^{-3} peak power under ambient conditions. The short power pulse resulted in a temperature increase from room temperature (RT) to around 390 °C, while cooling to 120 °C (limit of pyrometer) took around 190 ms. The corresponding heating and cooling rates (dT dt^{-1}) are depicted in Fig. 2h (bottom), with maximum values of 317,000 K s^{-1} and 40,000 K s^{-1}, respectively, which are 4 orders of magnitude higher compared to previous reports [6,10,16]. As revealed by the insets in Fig. 2h, there are three different regimes in the heating phase (0–1.7 ms). At first, the heating rate approaches a maximum after around 0.7 ms, followed by an almost constant plateau at ~190,000 K s^{-1} and a further steep decline at 1.6 ms, before the power is turned off. The different regimes correspond to the isochoric heating phase and the subsequent adiabatic gas expansion (refer to Fig. 1b). Furthermore, the heating rate can be adjusted by tuning the applied power pulse width (PPW). In Fig. S11, the Joule-heating characteristics of the F-AMs at constant energy input are shown for different power pulse durations.

In addition to the open-porous framework structure of the F-AMs, their extremely low volumetric heat capacity is crucial for the EPRAE process. To demonstrate that, we carried out comparative measurements between an Aero-EG sample (~4 mg cm^{-3}) and an EG/ZnO (~300 mg cm^{-3} / ~4 mg cm^{-3}) sample (non-etched EG-coated t-ZnO template), as shown in Fig. 2i. Both samples had a conductivity of ~8 S m^{-1}. The volumetric heat capacity of the Aero-EG can be estimated to be around ~6 kJ m^{-3} K^{-1} (Supplementary Text S1) while that of Aero-EG/ZnO is in the order of ~155 kJ m^{-3} K^{-1} and, thus, by a factor of ~26 higher. While heating of Aero-EG to 390 °C was achieved within 2.1 ms using an energy density of ~0.7 J cm^{-3}, a much higher energy density of ~14 J cm^{-3} (factor of 20) was required to heat the Aero-EG/ZnO sample to the same temperature. The large difference in the volumetric heat capacity can be best observed with respect to the cooling characteristics. While it takes only around 100 ms for Aero-EG to cool to 120 °C, the cooling of the EG/ZnO is by a factor of 10 longer (~1050 ms). Even slight changes in the density and, therefore, volumetric heat capacity of the F-AMs affect their heating and cooling characteristics and, thus, the EPRAE process (Supplementary Text S4).

Long-term stability of F-AMs during EPRAE

We further carried out long-term EPRAE measurements of up to 100,000 cycles between < 120 °C (limit of pyrometer) and ~400 °C as well as long-term (~12 h) steady-state measurements for different temperatures (Figs. S12 to S14) in order to study the stability of the F-AMs under these conditions. As shown in Fig. 3a, an Aero-rGO sample with a density of ~4 mg cm^{-3} is stable over 100,000 cycles (repetition rate 1 Hz) when subjected to a power pulses with a 1.5 ms PPW and a peak power density of ~200 W cm^{-3}, reaching a maximum temperature of 400 °C.

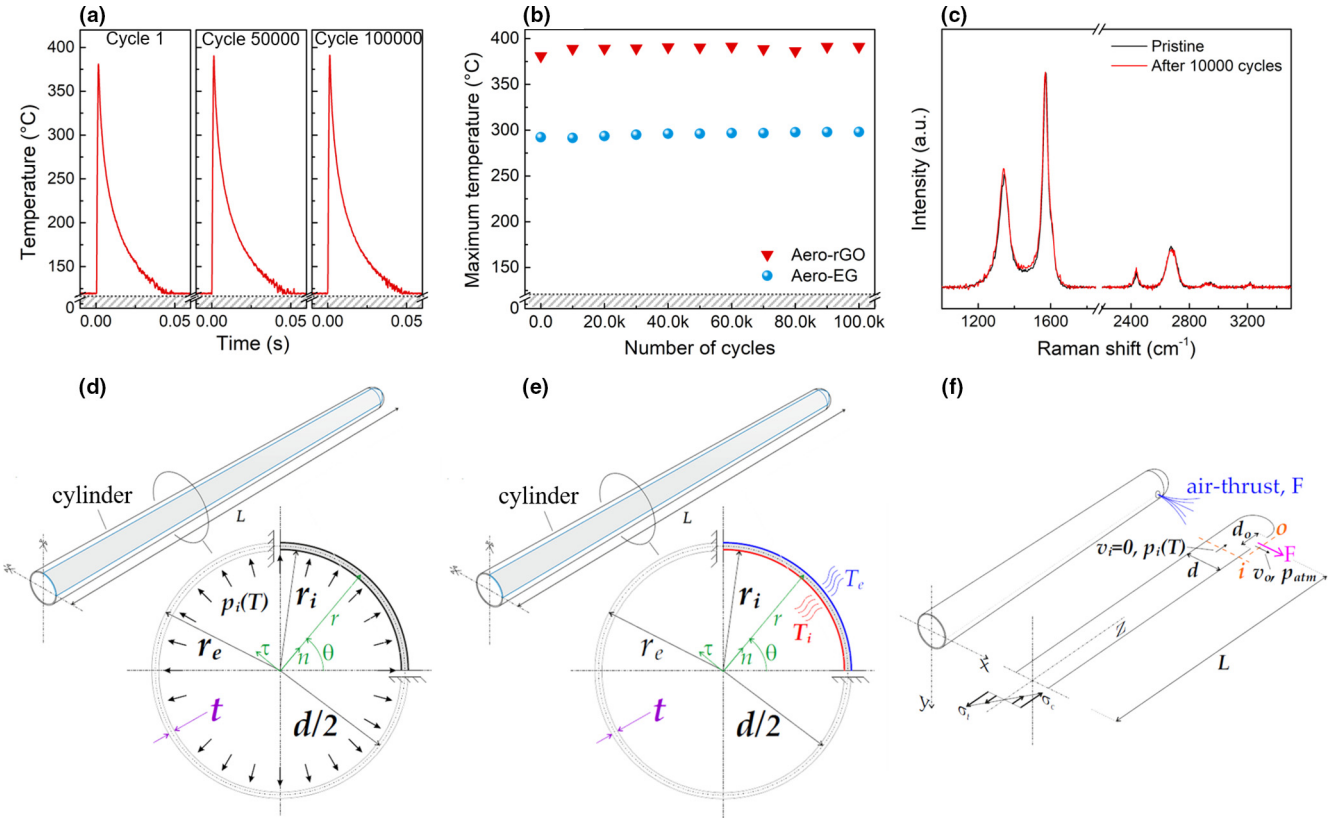

FIGURE 3

Long-term stability of EPRAE. (a) Temperature-time profiles for Aero-rGO (~4 mg cm^{-3}) during repetitive Joule-heating and cooling cycles, shown for the cycle 1, 50,000, and 100,000. (power pulse width = 1.5 ms; peak power density ~200 W cm^{-3}; repetition rate ~1 Hz.) (b) Evolution of maximum temperature over 100,000 EPRAE cycles, shown for Aero-rGO and Aero-EG. (c) *In situ* Raman spectra of Aero-EG before and after 10,000 EPRAE cycles. (d)–(f) Schematic of the analyzed failure mechanisms that could cause destruction of the F-AMs by the EPRAE process, i.e., (d) Hoop and longitudinal stress generated by air expansion inside the microtubes, (e) thermal stress caused by a temperature gradient between the inner and outer temperature of the microtube wall, and (f) longitudinal stress caused by airflow through the microtube voids.

The maximum temperature remained constant (Fig. 3b) and no change in the heating and cooling characteristics could be observed (Fig. 3a), indicating excellent long-term stability of Aero-rGO during EPRAE. Similarly, Aero-EG (density ~11 mg cm^{-3}) showed cycling stability over 100,000 cycles at a maximum temperature of ~300 °C and PPW of 1.3 ms (peak power density of ~190 W cm^{-3}), revealing constant heating and cooling characteristics (Fig. S12) as well as a constant maximum temperature (Fig. 3b). A photograph and SEM images of Aero-EG after 10,000 EPRAE cycles is presented in Fig. S15 and demonstrates the preservation of the macroscopic and microscopic structure. Additionally, *in situ* Raman measurements of Aero-EG demonstrated high chemical stability during cyclic Joule heating, as only minor changes in the spectra could be observed (Fig. 3c and Fig. S16). It should be noted that, despite its higher temperature stability compared to Aero-rGO, long-term EPRAE cycling of Aero-EG at 400 °C resulted in failure of the sample after a few 1000 cycles, evident by a temperature increase and change in cooling time (Fig. S13). We suspect that the lower stability of Aero-EG during EPRAE is caused by its lower mechanical stability compared to Aero-rGO [19]. The long-term constant Joule-heating characteristics (constant heating for a time period of 12 h) of Aero-rGO and Aero-EG are presented in Fig. S14.

Possible thermo-mechanical failure mechanisms resulting in the destruction of individual microtubes caused by the rapid heating of the F-AMs were investigated by analytical calculations and numerical simulations. In particular, three mechanisms have been identified (Fig. 3d–f): (M1) Hoop and longitudinal stress generated by a rapid air expansion inside the microtubes resulting in a pressure difference between the inside and the outside of the microtube (Fig. 3d), (M2) thermal stress caused by a temperature gradient between the inner and outer temperature of the microtube wall (Fig. 3e), and (M3) longitudinal stress caused by airflow through the microtube voids. The mechanisms are thoroughly discussed and analyzed in the Supplementary Information (Figs. S17 to S21 and Supplementary Text S5). The numerical and theoretical results suggest that the hollow microtubes most likely break by a combination of the mechanisms M1 and M2. The latter mechanism is suspected to be mainly responsible, with a Tresca maximal strength (shear strength) of the microtube on the order of 2–3 GPa, depending on the geometrical configuration (Tables S1–S4). We emphasize that the predicted stress is independent from the Young's modulus for the mechanism (A) and linearly dependent for the mechanism (B). Therefore, we suspect that the rapid volume expansions caused by the extremely fast temperature changes result in a structural damage (i.e., breaking of microtubes) over time. At constant volt-

age, a higher current will pass through the remaining microtubes of the F-AM network, causing an overall higher temperature and finally failure due to oxidation reactions. At even more extreme heating rates of $\sim 4 \cdot 10^6$ K s^{-1} (50 µs power pulses of 576 W, ΔT ~200 K) the complete F-AM starts to disintegrate, with macroscopic parts being pushed out from the structure, as shown in Video S2.

Rapid gas activation based on EPRAE

To obtain a deeper insight into the thermodynamic processes of individual EPRAEs, we measured the air volume expansion under isobaric conditions as well as air pressure changes under isochoric conditions as a function of the PPW. Therefore, an electrically connected F-AM was mounted into an air-tight chamber. For the isobaric system, two check valves were attached to the

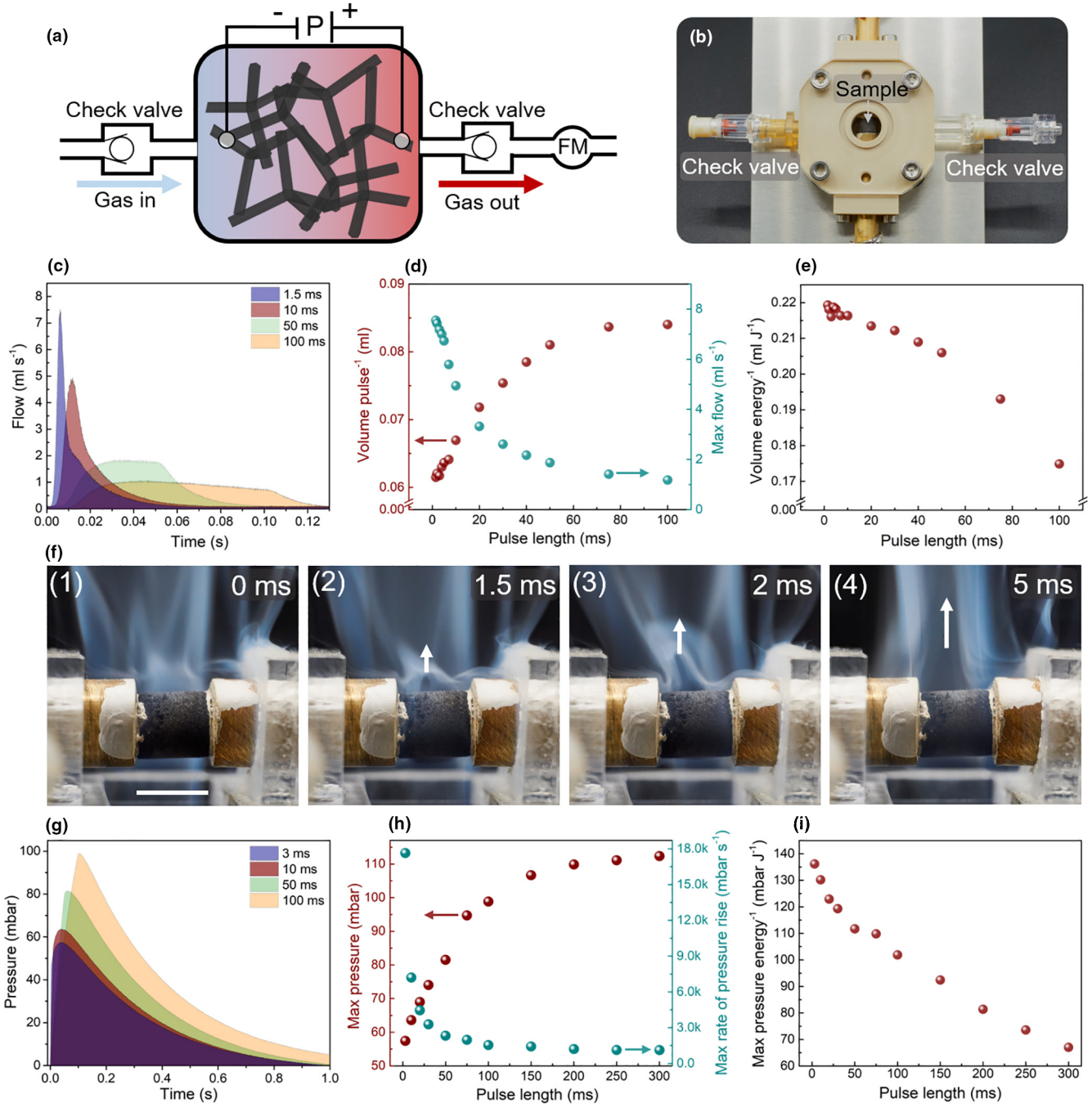

FIGURE 4

Rapid gas activation based on EPRAE. (a) Schematic of the measurement setup for the determination of the air volume expansion caused by EPRAE (P: power; FM: gas flow meter). For the pressure measurement, the right check valve and the flow meter were replaced by a pressure sensor. (b) Photograph of the employed measurement setup. (c) Air flow versus time for Aero-EG, resulting from EPRAEs to 400 °C at four different power pulse widths (PPWs). (d) Activated air volume per pulse and maximum air flow versus PPW. (e) Activated air volume normalized to the supplied energy versus PPW. (f) Sequence of photographs showing the EPRAE process. After applying a 1.5 ms power pulse to the sample, the heated air inside the F-AM expanded rapidly and displaced the surrounding smoke (white arrow) produced by an incense stick. Scale bar: 6 mm. (g) Pressure versus time for Aero-EG, resulting from EPRAEs to 350 °C at four different PPWs. (h) Maximum pressure and maximum rate of pressure rise versus PPW. (i) Maximum pressure normalized to the supplied energy versus PPW.

chamber to ensure air flow in only one direction (Fig. 4a and b). Thermodynamically, in case of an isobaric process, an increase in gas temperature is directly related to an increase in gas volume. In the given setup, the increase in air volume caused by an EPRAE induces an air flow through the right check valve, which is measured by a gas flow meter connected in series. The left check valve ensured pressure equalization after each heating pulse. The air flow induced by individual EPRAEs was measured as a function of PPW (1.5–100 ms), as shown in Fig. 4c. The maximum temperature was kept constant at 400 °C by adjusting the applied pulse power (Fig. S22). In the case of a pulse time of 1.5 ms, the air flow reaches a maximum of ~7.5 ml s^{-1}. As soon as the power is switched off, the air flow decreases rapidly to 0 (~70 ms). Increasing the PPW results in a decrease in the maximum air flow but a longer overall air flow, as shown in Fig. 4c. With increasing PPW, the maximum air flow decreases from ~7.5 ml s^{-1} to ~1.6 ml s^{-1}, while the activated air volume per pulse increases from ~0.065 ml to ~0.085 ml, at 1.5 ms and 100 ms PPW, respectively (Fig. 4d). For PPWs > 75 ms, the volume per pulse approaches an upper limit of 0.085 ml. Assuming ideal gas behavior, the air contained inside the F-AM (volume ~0.16 ml) should expand to a volume ~0.37 ml at a temperature change from 20 °C to 400 °C, causing a total air flow of ~0.21 ml. Considering the upper limit of 0.085 ml, the efficiency of the system is ~41 %. The detailed calculation of the pump efficiency is presented in the Supplementary Text S5.

We suppose measured value of 0.085 ml is caused by the fact that the bulky metal contacts act as a heat sink, resulting in lower heating of the sample close to the contact surface, similar to what was reported for the heating of other carbon nanomaterial assemblies [6]. Additionally, an optimized experimental setup could contribute to an increased efficiency. Nevertheless, the measurements demonstrate that a large part of the gas contained inside the F-AMs can be rapidly and reversibly activated by the EPRAE process, e.g. ~40% in 1.5 ms. Activating a higher percentage would be possible by further increasing the surface area or the density of the F-AMs. However, this would have direct consequences on the gas transport inside the F-AMs during EPRAE (see Supplementary Text S4). With respect to energy consumption, the EPRAE process is more efficient the lower the PPW (Fig. 4e), with a maximum value of ~0.22 ml J^{-1} at 1.5 ms. With increasing PPW, the value decreases to ~0.17 ml J^{-1} for 100 ms PPW. This behavior can be understood as follows. In the first heating stage the gas close to the microtubes of the F-AMs is rapidly heated. Heating of the gas volume further away from the microtubes is accomplished by heat transfer within the gaseous phase, which requires more time compared to the heating of the initial gas volume. The air expansions caused by a 1.5 ms EPRAE to ~400 °C is visualized in the photographs shown in Fig. 4f (and Video S1). The smoke (produced by an incense stick) surrounding the F-AM is rapidly pushed away by a single EPRAE.

We further investigated the change in air pressure caused by individual EPRAEs in the chamber by replacing the right check valve by a pressure sensor, providing an isochoric system. Thermodynamically, in case of an isochoric process, an increase in gas temperature scales linearly with an increase in gas pressure, as shown in Fig. S23 for a F-AM, which was heated to different temperatures between 150 °C and 400 °C at a constant PPW. The obtained pressure–time curves for different PPWs (3–100 ms) are shown in Fig. 4g. Please note that the shortest PPW is slightly longer (3 ms) compared to the air flow measurement shown in Fig. 4c (1.5 ms). This is due to the use different samples with slightly differing resistances and the limitation of the voltage supply (29 V), resulting in small differences in the shortest possible time to heat the samples to ~400 °C. The maximum temperature was kept constant at 350 °C by adjusting the applied power (Fig. S22). In the case of 3 ms PPW, the air pressure in the chamber reached a maximum of ~56 mbar (in addition to the standard pressure). As soon as the power was switched off, the pressure decreased down to its original value (~1 s). Increasing the PPW of the EPRAE resulted in an increase in the maximum pressure, e.g., 104 mbar at 300 ms PPW (Fig. 4h). For PPWs > 150 ms, the maximum pressure approached an upper limit. The slight increase in maximum pressure for PPWs > 150 ms is most likely caused by the heating of the air surrounding the F-AM. The maximum rate of pressure rise, a number used to describe explosions, decreased with increasing PPW (Fig. 4h), with a maximum value of ~18 bar s^{-1} for a PPW of 3 ms. In Fig. 4h, the maximum pressure is plotted as a function of supplied energy, indicating that shorter EPRAE PPWs are more efficient. The results are in accordance with the once obtained from the measurements under isobaric conditions.

Applications of EPRAE

The measurements shown in Fig. 4 demonstrate that the EPRAE process enables ultrafast (few ms) and repeatable activation of macroscopic gas volumes, which can be exploited for a broad variety of applications (Fig. 5), such as micro-pumps for fluidics, rapid micro-actuators, micro-thrusters, as well as thermophones. Fig. 5a shows a schematic of the different working principles. As shown in Fig. 5b, a rapid succession of EPRAEs at a repetition rate of 6.25 Hz was exploited to pump a fluid through a glass capillary. The corresponding flow rate versus time profile is shown in Fig. 5c. As revealed by the magnification between 5 and 6 s in Fig. 5d, peak values of 400 °C and 160 ml min^{-1} were obtained for the temperature and air flow, respectively. The corresponding Video S3 shows the step-like movement of the fluid, where each step represents an individual heating pulse. The pumping rate of the micro-pump can be controlled by changing the EPRAE process parameters. It is proportional to the change in temperature (and, thus, power), the repetition rate (power pulse frequency), and the power pulse width and can be tuned on the fly. An almost constant gas flow of 9 ml min^{-1} (~60 ml min^{-1} cm^{-3} normalized to the volume of the F-AM) could be achieved by cycling the system between ~400 °C and ~200 °C at a 5 ms power pulse duration and frequency of ~9.5 Hz (Fig. S24). In contrast to conventional miniature gas pumping systems, which rely on oscillating membranes, our system is free of any mechanical moving parts (except for the check valves). Furthermore, existing gas pumping systems that do not require mechanical moving parts, such as Knudsen pumps [31] (thermal transpiration pump), usually have very low specific pumping rates on the order of ~0.03 ml min^{-1} cm^{-3} [31], a factor of ~2000 lower compared to what is reported here. In terms of energy consumption, the EPRAE-based pump outperforms Knudsen pumps by 2 orders of

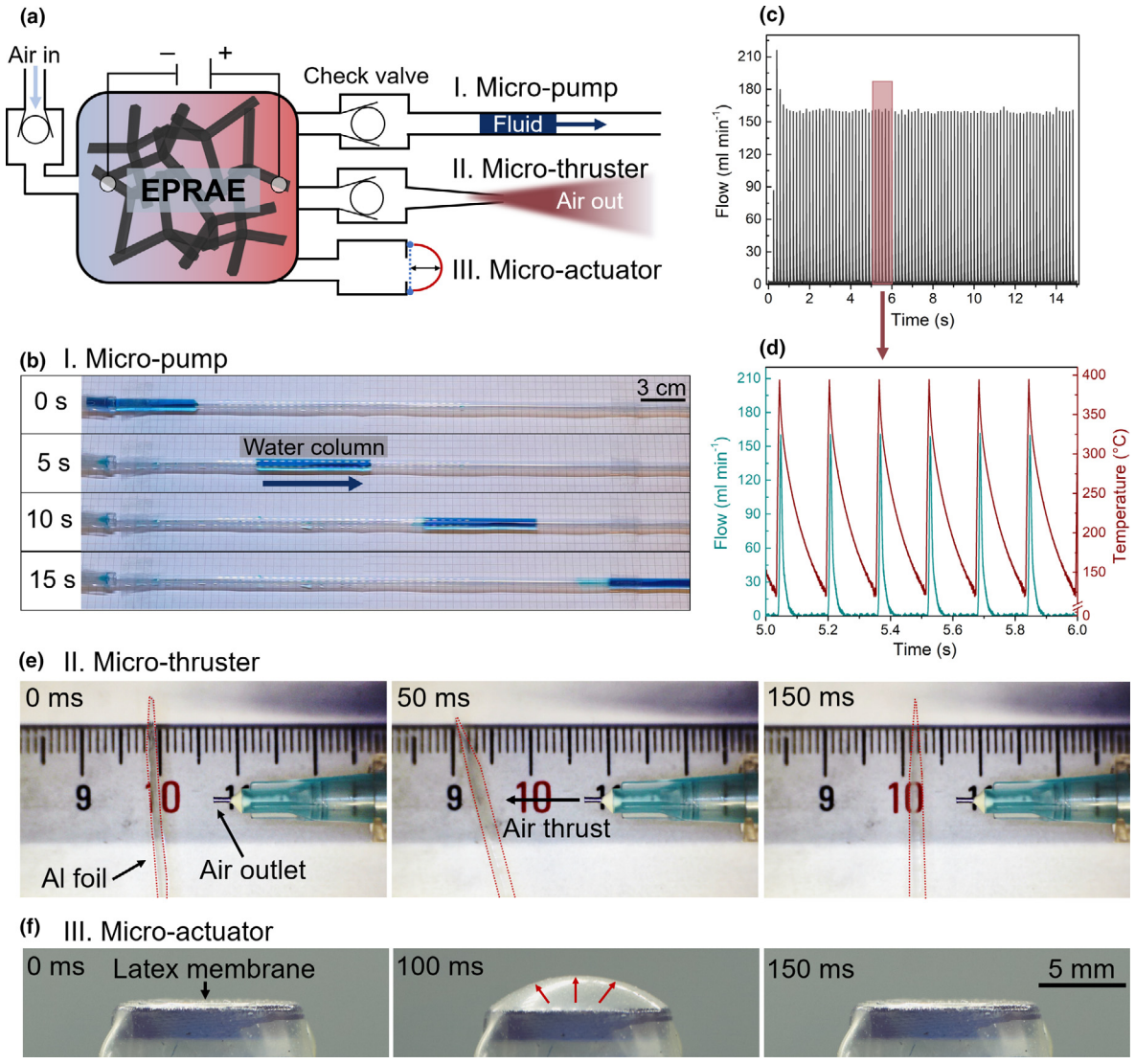

FIGURE 5

EPRAE Applications. (a) Schematic illustration of three EPRAE applications: I. micro-pump, II. Micro-thruster and III. Micro-actuator. The corresponding videos of the applications are shown in Video S3. (b) Sequence of photographs showing the exploitation of a sequence of EPRAEs for pumping a fluid through a glass capillary. (c) Corresponding air flow versus time to the photographs shown in B. The EPRAE repetition rate is 6.25 Hz with a peak power of ~16.5 W and a PPW of 10 ms. The range between 5 and 6 s is magnified in (d) and complemented by the corresponding temperature–time profile. (e) Sequence of photographs showing the rapid creation of an air thrust moving a thin aluminum foil induced by a single EPRAE (PPW of 50 ms, peak power ~26.5 W) A photograph of the setup is shown in Fig. S23. (f) Sequence of photographs showing the rapid micro-actuation of a rubber membrane, induced by a single EPRAE (PPW of 100 ms, peak power ~10 W).

magnitude, with ~0.47 ml min^{-1} cm^{-3} W^{-1} and ~51.25 ml min^{-1} cm^{-3} W^{-1}, respectively. In addition to microfluidic pumping systems, the explosion-like air expansion produced by EPRAE can also be employed in the scope of lightweight, highly precise and rapid micro-thrusters (Fig. 5e and Video S3, photograph of setup in Fig. S25), e.g., for the use in resistojets for micro propulsion systems of satellites [32]. Same as for the micropumps, the thrust can be controlled by the EPRAE process parameters. Based on their low volumetric heat capacity and microstructure, the demonstrated F-AMs are also ideal candidates for omnidirectional thermophones. As shown in Fig. S26A and Video S3, a common in-ear headphone casing was equipped with a F-AM (cylindrical geometry with a diameter of 6 mm and a height of 5 mm) to emit sound over a broad frequency range by using a conventional tablet. The change in temperature for different applied frequencies can be seen in Fig. S26B, indicating that even high frequencies of 500 Hz induce large temperature fluctuations of more than 2 K. These properties can also be used for highly sensitive gas flow meters showing an exponential decay of the maximum temperature with increasing gas flow (details in Fig. S27), as even small air movements such as clapping have a direct effect on the temperature of the F-AMs (Video S5).

Furthermore, the EPRAE concept can be used for the fabrication of rapid, lightweight and repeatable pneumatic micro- and macro-actuators, that do not require any external pressure source, which makes them highly interesting for soft robotics [33–35]. As shown in Fig. 5f and Video S3, a thin latex membrane

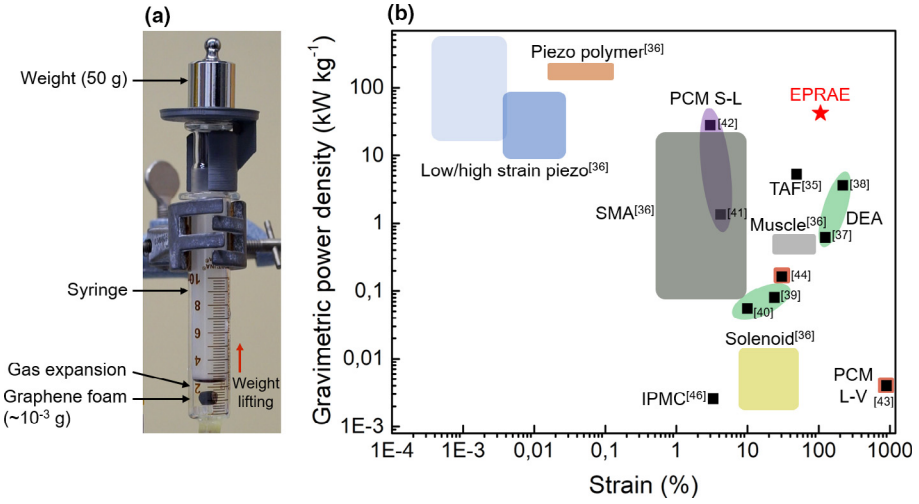

FIGURE 6

EPRAE-based actuator. (a) Photograph of EPRAE-based actuator consisting of a glass syringe with an integrated lightweight F-AM (~1.5 × 10–6 kg), employed for actuation of a weight (0.05 kg) within ~10 ms. The weight is lifted due to the gas volume expansion (106% with respect to the volume of the F-AM) caused by the EPRAE. The corresponding video is shown in the Supplementary Information (Video S4). (b) Gravimetric power density versus strain for various electrically powered actuator systems and the introduced EPRAE-based actuator. SMA: shape memory alloy, PCM: phase change material solid–liquid (S-L)/liquid–vapor (L-V), DEA: dielectric elastomer actuator, IPMC: ionic polymer metal composite, TAF: thermally activated fiber.

on top of a closed housing containing the F-AM could be repeatedly expanded at a high repetition rate by the EPRAE inside the chamber, demonstrating the potential for application in soft robotics.

EPRAE-based high-power actuator

Moreover, the EPRAE process enables actuator systems which show both high gravimetric power densities and large volume expansions. As demonstrated in Fig. 6a (details in Video S4), a F-AM with a weight of ~1.5 mg can rapidly and repeatedly actuate a weight of 65 g by ~1 mm in height (syringe diameter of ~1.5 cm) in ~0.01 s. It should be noted, that this experiment has been carried out using nitrogen as working gas in order to increase the possible temperature range. Even this unoptimized setup demonstrates that EPRAE-based actuators enable fast and large volumetric (~100% with respect to the volume of the F-AM) movements with output power densities (output power normalized to the weight of the transducer material) of ~40 kW kg^{-1}. Please note that the concept allows to increase systems inner energy by pre-compression and thus adopts easily to highest loads. As demonstrated in Video S4, even a weight of 2 kg can be lifted in 0.025 s by 2.2 mm, resulting in power densities >1000 kW kg^{-1} at 235% strain. In principle, even higher power densities can be reached, as the EPRAE actuator system is only limited by the stability of the F-AM, that can withstand even extreme heating rates of ~10^6 K s^{-1} (see Video S2) and the mechanical stability of the surrounding container. Generally, the F-AM did not show any mechanical degeneration during the weigh-lifting experiments, confirming the cycling stability demonstrated in Fig. 3. In comparison to other electrically driven actuator systems (Fig. 6b), the EPRAE process is capable of providing both a high strain and power density, thereby outperforming state-of-the-art actuator systems, e.g., based on shape memory alloys [36], piezo polymers [36], dielectric elastomers [37–40], and phase change materials [41–44]. In the future, soft robots that were limited by pneumatic tethers [45] or relied on irreversible combustion reactions [46], can be powered using the demonstrated EPRAE concept. Additionally, this concept could be further extended to fabricate electrically powered small-scale heat engines that can be operated at ambient conditions, as well as active and adaptive gas springs or dampers.

Conclusions

In summary, we introduced a new process that enables electrically powered repeatable air explosions utilizing graphene-based F-AMs. The concept is based on the framework structure of the graphene foams featuring large and open pores, which, in contrast to classical aerogels, allows for extremely fast (few ms) heating and cooling of macroscopic gas volumes. A broad range of sectors will benefit from the here introduced EPRAE concept. In microfluidics, the EPRAEs can be used for precise pumping, rapid switching of valves, rapid micro-actuators allowing for large and efficient volume changes (different to piezo-based systems), as well as micro-engines. Second, the EPRAE concept enables lightweight pneumatic systems on demand, useful for mobile applications, e.g. tactile displays and soft robotics, as well as pneumatic shock absorbers and car breaks. Additionally, basically all areas that require rapid activation of gases, such as in catalysis (e.g., by functionalizing the F-AMs with other nanomaterials), sensing, sorption and thermoacoustics (e.g., flat and omnidirectional loudspeakers) can benefit from the introduced concept. There are several other potential opportunities, including propulsion systems like thrusters used in satellites.

The EPRAE concept can be further extended by (I) the use of inert gases, such as nitrogen, which allow for even higher maximum temperatures (more than 3000 °C) and, thus, pressures/volume expansions that can be reached, and (II) increasing the compression ratio like in every combustion engine to obtain a multiple of pressure increase and volume expansion for the same

temperature difference. Thus, the EPRAE concept holds promise to reach Carnot efficiencies of more than 90%, which is unique for heat engines and close to that of conventional electrical engines.

Declaration of Competing Interest

The authors declare that they have no known competing financial interests or personal relationships that could have appeared to influence the work reported in this paper.

Acknowledgements

R.A., F.R., and F.S. acknowledge funding by the Deutsche Forschungsgemeinschaft (DFG) under contracts AD183/27-1, AD 183/18-1 and GRK 2154 and the Volkswagen Foundation in the scope of funding initiative "Experiment!" under contract A131464. This project has received funding from the European Union's Horizon 2020 Research and Innovation Programme under grant agreement No GrapheneCore2 785219, GrapheneCore3 881603, the FET Proactive ("Neurobres") grant No. 732344, the FET Open ("Boheme") grant No. 863179.

Author contributions

R.A., F.S., and F.R. developed the EPRAE concept. F.S., F.R., N.M.P, and R.A. designed the study. A.R.V., A.S.N., and M.R.L. prepared the nanomaterial dispersions (EG and GO) and the graphene aerogel. F.R., F.S., N.D., L.M.S., and A.R. fabricated the samples and carried out the Joule heating experiments. S.K., F.S. and F.R. constructed the experimental setup for the Joule heating characterization of the samples. S.K., F.S., A.R., and J.R. constructed the experimental setup for the gas flow and pressure measurements. F.S., F.R., J.R., S.K., L.M.S. and A.R. constructed the demonstration setups for the loudspeaker, micro-actuator, gas flowmeter, and thruster. F.S., F.R. N.D., and R.A. analyzed the data. F.R. performed the SEM and Raman characterization of the samples. D.M. and N.M.P. developed the mechanical modelling of the failure mechanisms, conducted the simulations of the failure mechanisms and analyzed the data. F.S., F.R., Y.K. M., R.A., A.S.N., M.R.L. X.F. and J.C., finalized the study and wrote the paper. All of the authors have contributed to the discussion of the results and reviewed the manuscript.

Data availability

The data that support the findings of this study are available from the corresponding authors upon request.

Competing interests

A patent application (DE102020110746.3) has been submitted based on these results.

Appendix A. Supplementary data

Supplementary data to this article can be found online at https://doi.org/10.1016/j.mattod.2021.03.010.

References

[1] R. Pape, K.R. Mniszewski, A. Longinow, Pract. Period. Struct. Des. Constr. 15 (2010) 135–140.
[2] K. Wüthrich, Chimia (aarau) 57 (2003) 757–765.
[3] Appendix A: Explosion and Fire Phenomena and Effects, in: Guidelines for Evaluating Process Plant Buildings for External Explosions and Fires, John Wiley & Sons, Ltd, 2010, pp. 131–148.
[4] K. Terao, Irreversible phenomena in ignitions, combustion and detonation waves, Springer, Berlin, London, 2007.
[5] M. Sakr, S. Liu, Renew. Sustain. Energy Rev. 39 (2014) 262–269.
[6] R. Menzel et al., Adv. Funct. Mater. 25 (2015) 28–35.
[7] D. Xia, H. Li, P. Huang, Nanoscale Adv. (2020).
[8] D. Xia et al., Chem. Commun. 56 (2020) 14393–14396.
[9] F. Yavari et al., Sci. Rep. 1 (2011) 166.
[10] Q. Zhang et al., J. Mater. Sci. 53 (2018) 528–537.
[11] W. Fei, J. Zhou, W. Guo, Small (Weinheim an der Bergstrasse, Germany) 11 (2015) 2252–2256.
[12] C.S. Kim et al., ACS Appl. Mater. Interfaces 8 (2016) 22295–22300.
[13] F. Giorgianni et al., Adv. Funct. Mater. 28 (2018) 1702652.
[14] A.K. Samantara, S. Ratha, S. Raj, Functionalized graphene nanocomposites in air filtration applications, in: A.E.K. Qaiss, M. Jawaid, R. Bouhfid (Eds.), Functionalized graphene nanocomposites and Their Derivatives: Synthesis, Processing and Applications, Elsevier Ltd, Amsterdam, Netherlands, 2019, pp. 65–89.
[15] Y. Xie et al., ACS Nano 13 (2019) 5385–5396.
[16] J. Ge et al., Nat. Nanotechnol. 12 (2017) 434–440.
[17] A.K. Geim, K.S. Novoselov, Nat. Mater. 6 (2007) 183–191.
[18] K. Shehzad et al., Three-dimensional macro-structures of two-dimensional nanomaterials, Chem. Soc. Rev. 45 (2016) 5541–5588.
[19] F. Rasch et al., ACS Appl. Mater. Interfaces 11 (2019) 44652–44663.
[20] R. Meija, et al., Nat Commun 8; 1–9.
[21] Engineering thermodynamics, McGraw Hill Education (India) Private Limited, Chennai, 2018.
[22] F. Schütt, et al., Nat. Commun. 8; 1–10.
[23] ZnO tetrapod materials for functional applications, Materials Today 21 (2018) 631–651.
[24] X. Zhang et al., J. Mater. Chem. 21 (2011) 6494–6497.
[25] K. Huang et al., Adv. Mater. Interfaces 5 (2018) 1701299.
[26] Thickness-dependent thermal resistance of a transparent glass heater with a single-walled carbon nanotube coating, Carbon 49 (2011) 1087–1093.
[27] M.A. Aegerter, N. Leventis (Eds.), Aerogels Handbook, Springer Science +Business Media LLC, New York, NY, 2011.
[28] Y. Xie et al., Carbon 98 (2016) 381–390.
[29] A. Passian et al., Ultramicroscopy 97 (2003) 401–406.
[30] S.G. Jennings, J. Aerosol Sci. 19 (1988) 159–166.
[31] N.K. Gupta, Y.B. Gianchandani, Appl. Phys. Lett. 93 (2008).
[32] M.N. Sweeting, T. Lawrence, J. Leduc, Low-cost orbit manoeuvres for minisatellites using novel resistojet thrusters, Proc. Inst. Mech. Eng., Part G: J. Aerospace Eng. 213 (1999) 223–231.
[33] M. Wehner et al., Nature 536 (2016) 451–455.
[34] J. Walker et al., Actuators 9 (2020) 3.
[35] C.S. Haines et al., Science 343 (2014) 868–872.
[36] J.E. Huber, N.A. Fleck, M.F. Ashby, Proc. R. Soc. Lond. A 453 (1997) 2185–2205.
[37] E. Acome et al., Science 359 (2018) 61–65.
[38] J.D.W. Madden et al., IEEE J. Ocean. Eng. 29 (2004) 706–728.
[39] M. Duduta, et al. Proc. Natl. Acad. Sci. U.S.A. 116 (2019) 2476–2481.
[40] H. Zhao et al., Adv. Funct. Mater. 28 (2018) 1804328.
[41] J.I. Lipton, Adv. Eng. Mater. 18 (2016) 1710–1715.
[42] M.D. Lima et al., Science 338 (2012) 928–932.
[43] A. Miriyev, K. Stack, H. Lipson, Nat. Commun. 8; 1–8.
[44] J.-H. Jeong et al., Nanoscale Adv. 1 (2019) 965–968.
[45] S.I. Rich, R.J. Wood, C. Majidi, Nat. Electron. 1 (2018) 102–112.
[46] N.W. Bartlett, Science 349 (2015) 161–165.